

---

# Simulation of Solar Radiative Magneto-Convection

M. Schüssler<sup>1</sup>, J.H.M.J. Bruls<sup>2</sup>, A. Vögler<sup>1</sup>, and P. Vollmöller<sup>1,3</sup>

<sup>1</sup> Max-Planck-Institut für Sonnensystemforschung  
Max-Planck-Str. 2, 37191 Katlenburg-Lindau, Germany  
[schuessler@linmpi.mpg.de](mailto:schuessler@linmpi.mpg.de)

<sup>2</sup> Kiepenheuer-Institut für Sonnenphysik  
Schöneckstr. 6, 79104 Freiburg, Germany  
[bruls@kis.uni-freiburg.de](mailto:bruls@kis.uni-freiburg.de)

<sup>3</sup> Present address: VAW, ETH-Zentrum, 8092 Zürich, Switzerland

## 1 Introduction

The term ‘magneto-convection’ summarizes the variety of processes arising from the dynamic interaction between convective motions and magnetic fields in an electrically conducting medium. Magneto-convective processes play an important role in many astrophysical systems; their effects can be best studied in the case of the Sun, where the relevant spatial and temporal scales of the phenomena can (in principle, at least) be observed. The generation of magnetic flux in the Sun by a self-excited dynamo process and the various spectacular phenomena of solar activity, like sunspots, coronal loops, flares, and mass ejections all are, directly or indirectly, driven by magneto-convective interactions.

The large length scales of the typical convective flow structures on the Sun lead to high (hydrodynamic and magnetic) Reynolds numbers, so that the magneto-convective processes typically involve nonlinear interactions and formation of structures and patterns. Fig.1 illustrates typical regimes of magneto-convection near the visible solar surface, differing mainly in the amount of magnetic flux per unit area (i.e., average magnetic field strength) and the orientation of the field. In the ‘quiet’ Sun, some magnetic flux is concentrated in bright *magnetic elements*, isolated patches with field strengths exceeding 1000 G (corresponding to 0.1 Tesla). In magnetically active regions, such magnetic elements densely populate the dark convective downflow network and decrease the size of convective upflows (‘granules’ in solar physics lingo). In the dark core of a sunspot (the so-called umbra), the strong vertical magnetic field is space-filling and largely suppresses the convective energy transport. The less dark, striated periphery of a sunspot (the penumbra) har-

bors a magnetic field which is strongly inclined with respect to the vertical direction.

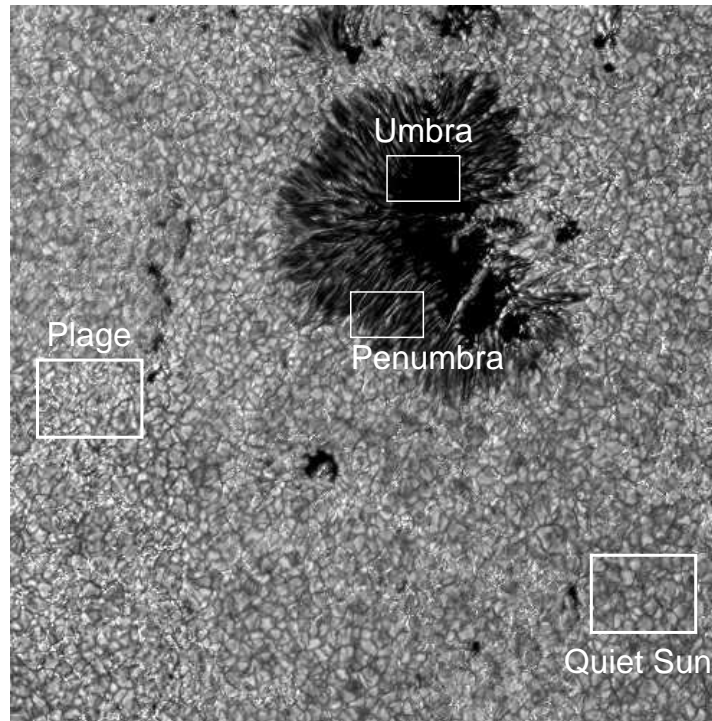


**Fig. 1.** Magnetic structure on the visible solar surface and different regimes of magneto-convection. There is only a small amount of magnetic flux in quiet regions and the convective pattern (hot plasma rising in bright ‘granules’, cooled by radiation and flowing back into the interior in the network of dark intergranular lanes) is best visible. In areas with more magnetic flux (plage regions), the flux becomes assembled in small flux concentrations, which appear bright because of locally enhanced transparency of the atmosphere. At even higher levels of magnetic flux density, the convection is largely suppressed by the magnetic field and sunspots form. They have a dark core (the umbra) with almost vertical magnetic field and a surrounding region of inclined field (the penumbra), whose striated appearance and mode of energy transport are not well understood (Image taken with the German Vacuum Tower Telescope on Tenerife, Spain, operated by the Kiepenheuer-Institut, Freiburg; courtesy O. von der Lühe)

Realistic numerical simulations of solar magneto-convection represent a considerable computational challenge. There is an extended range of length scales between the dominant scale of the convective flow pattern (the granulation) of about  $10^3$  km and the dissipation scales of the order of a few km and less. The plasma is strongly stratified with pressure scale heights down

to about 100 km and even a restricted simulation has to cover a density ratio of the order of 100. Convective velocities reach the sound speed, so that full compressibility is mandatory. Solar convection is strongly affected by partial ionization effects and over some height range near the surface the major part of the convective energy flux is transported in the form of latent heat. Consequently, the ionization state of the most abundant species (foremost hydrogen) has to be monitored in the course of the simulation and the related energetics have to be incorporated into the equation of state, which then cannot be written as a closed expression but has to be specified in the form of a numerical table.

The energetics of the lower solar atmosphere is strongly affected by radiative energy transport. In this region, radiative heating or cooling of the plasma cannot be considered as a local (diffusive) process since the mean free path of photons is comparable to or larger than the dominant spatial scale of the flow patterns and the pressure scale height. Consequently, the radiative transfer equation for the specific intensity of radiation has to be integrated along a large number of rays of various angles in order to determine the radiation incident on each grid cell. In order to correctly represent the temperature field in the solar atmosphere, the frequency dependence of the radiation has to be taken into account. This further complicates the problem because about a million spectral lines contribute to the energy balance in the solar photosphere.

Another complication is related to the boundary conditions. Because of the strong stratification and large size of the solar convection zone, the computational box for any realistic simulation of solar convection can only cover a tiny fraction of the whole convection zone and solar surface. Therefore, we have numerical boundaries where physically no boundaries are. For the side boundaries one can assume periodic conditions if the box is much larger than the dominant scale of the flow, but for the top and bottom boundaries the situation is less clear in a gravitationally stratified medium. Particularly at the bottom the assumption of a closed boundary would be quite unrealistic: in compressible convection, the downflows are narrow, fast and coherent over many scale heights. It is thus necessary to develop appropriate ‘open’ boundary conditions, which permit the free in- and outflow of matter while maintaining the total mass in the computational box and allowing for the correct amount of convective energy transport.

In order to meet the computational and methodological challenges, our ANumE project had three major goals:

1. Develop and evaluate methods to treat frequency-dependent radiative energy transport in simulations of magnetohydrodynamic processes,
2. develop combined compressible MHD/radiative transfer codes with partial ionization and open boundaries, and

3. perform realistic simulations and analyze them with spectral and polarization diagnostics in order to compare with observations and measurements of the Sun.

The whole project is carried out in close cooperation with our colleagues A. Dedner, M. Wesenberg, Christian Rohde, and D. Kröner from the Institute for Applied Mathematics (IAM) of the University of Freiburg. It proved to be fruitful to develop two codes more or less in parallel. One development (mainly by the IAM group) concerned a code based upon MHD Riemann solvers for non-ideal gases, an unstructured grid with adaptive grid refinement and dynamical load balancing for parallel computation. The second code was developed in cooperation with F. Cattaneo, Th. Emonet, and T. Linde from the University of Chicago; it is less sophisticated (fixed structured grid, 4th-order finite-differences and time stepping) and thus was available in 3D somewhat earlier than the IAM code, so that the developed methods and modules for non-grey radiative transport (RT) could be incorporated and tested, including first full simulation runs. A 2D version of the IAM code has been already combined with the RT; for the 3D version this is currently been done and first results are expected in 2004.

This paper is organized as follows. We briefly describe the basic equations of radiative MHD in Sec. 2. The developments of numerical methods for radiative transfer are discussed in Sec. 3: RT on unstructured grids in Sec. 3.2 and the treatment of the frequency dependence in Sec. 3.3. Results of simulations are presented in Sec. 4: first results of 2D simulations with the IAM code combined with RT are shown in Sec. 4.1 while 3D results with the MPAe-Chicago code and non-grey RT are given in Sec. 4.2. We conclude with a brief outlook in Sec. 5.

## 2 Equations of radiative magnetohydrodynamics

The magnetohydrodynamic (MHD) approximation can be used to describe a collision-dominated, electrically well-conducting, quasi-neutral plasma. These conditions are fairly well fulfilled in the convection zone and lower atmosphere of the Sun. Starting from the Maxwell equations (in Gaussian units),

$$\nabla \times \mathbf{B} = \frac{4\pi}{c} \mathbf{j} + \frac{1}{c} \frac{\partial \mathbf{E}}{\partial t}, \quad (1)$$

$$\nabla \times \mathbf{E} = -\frac{1}{c} \frac{\partial \mathbf{B}}{\partial t}, \quad (2)$$

$$\nabla \cdot \mathbf{E} = 4\pi\epsilon, \quad (3)$$

$$\nabla \cdot \mathbf{B} = 0, \quad (4)$$

with the electric field  $\mathbf{E}$ , the magnetic field  $\mathbf{B}$ , current density  $\mathbf{j}$ , and electrical charge density  $\epsilon$ , the MHD approximation is obtained under the assumptions

that all material speeds and phase velocities are small compared to the speed of light and that the plasma can be considered to be charge-neutral owing to a sufficiently high electrical conductivity. These conditions entail that the electrical field is small compared to the magnetic field and that the displacement current (second term on the right-hand side of (1)) can be neglected. Using Ohm's law in a medium locally moving with velocity  $\mathbf{v}$ ,

$$\mathbf{j} = \sigma(\mathbf{E} + \frac{1}{c}\mathbf{v} \times \mathbf{B}), \quad (5)$$

where  $\sigma$  is the electrical conductivity, we derive a single equation for the time evolution of the magnetic field, the *induction equation*, viz.

$$\frac{\partial \mathbf{B}}{\partial t} = \nabla \times (\mathbf{v} \times \mathbf{B}) - \nabla \times (\eta \nabla \times \mathbf{B}), \quad (6)$$

with the magnetic diffusivity defined as  $\eta = c^2/4\pi\sigma$ . The induction equation governs the time evolution of the magnetic field for a given velocity field,  $\mathbf{v}$ . The first term on the r.h.s. describes the inductive effect of the velocity field, the second term accounts for diffusion of magnetic field due to the finite conductivity of the plasma. The order-of-magnitude estimate for the ratio of these terms gives the *magnetic Reynolds number*,  $R_m = vL/\eta$ , where  $v$  is a typical speed and  $L$  is a typical length scale of the flow under consideration. Estimates for the photosphere and upper convection zone give magnetic Reynolds numbers of the order of  $10^5 - 10^6$ , so that the diffusion term is almost negligible in these regions. In the high- $R_m$  regime, *Alfven's theorem of flux-freezing* applies: magnetic field lines are transported by the fluid as if frozen in and fluid motions relative to the magnetic field are possible only along the direction of field lines.

The rest of the equations of the MHD approximation are the equations of hydrodynamics with appropriate magnetic terms in the momentum equation (the Lorentz force) and the energy equation (the Joule dissipation term in the case of a non-vanishing magnetic diffusivity). The continuity equation

$$\frac{\partial \varrho}{\partial t} + \nabla \cdot (\varrho \mathbf{v}) = 0 \quad (7)$$

represents mass conservation. The equation of motion is written in momentum conservation form:

$$\frac{\partial \varrho \mathbf{v}}{\partial t} + \nabla \cdot \left[ \varrho \mathbf{v} \mathbf{v} + \left( p + \frac{|\mathbf{B}|^2}{8\pi} \right) \mathbf{1} - \frac{\mathbf{B} \mathbf{B}}{4\pi} \right] = \varrho \mathbf{g} + \nabla \cdot \underline{\underline{\tau}}. \quad (8)$$

Here  $p$  is the gas pressure and  $\mathbf{g}$  the vector of gravitational acceleration.  $\mathbf{v} \mathbf{v}$  and  $\mathbf{B} \mathbf{B}$  are dyadic products and  $\mathbf{1}$  is the  $3 \times 3$  unit matrix. The magnetic force (Lorentz force) has been split into the gradient of the magnetic pressure,  $p_{\text{mag}} = |\mathbf{B}|^2/8\pi$ , and the term  $-\nabla \cdot (\mathbf{B} \mathbf{B}/4\pi)$ , which represents a tension along magnetic field lines. The last term on the r.h.s. of (8) is the viscous force, written as divergence of the viscous stress tensor,  $\underline{\underline{\tau}}$ .

The energy equation is written in the form

$$\begin{aligned} \frac{\partial e}{\partial t} + \nabla \cdot \left[ \mathbf{v} \left( e + p + \frac{|\mathbf{B}|^2}{8\pi} \right) - \frac{1}{4\pi} \mathbf{B}(\mathbf{v} \cdot \mathbf{B}) \right] \\ = \frac{1}{4\pi} \nabla \cdot (\mathbf{B} \times \eta \nabla \times \mathbf{B}) + \nabla \cdot (\mathbf{v} \cdot \underline{\underline{\tau}}) + \nabla \cdot (K \nabla T) \\ + \varrho(\mathbf{g} \cdot \mathbf{v}) + Q_{\text{rad}}. \end{aligned} \quad (9)$$

for the total energy density per unit volume,  $e$ , which is the sum of internal, kinetic and magnetic energy densities.  $T$  is the temperature and  $K$  the thermal conductivity.  $Q_{\text{rad}}$  is the radiative source term which accounts for heating and cooling of the plasma by radiation. This term is discussed in detail in Sec. 3.

In order to close the system of MHD equations, we have to specify a relation between pressure,  $p$ , density,  $\varrho$ , and internal energy of the gas,  $e_{\text{int}}$ . At temperatures typically encountered in the photosphere and upper convection zone, the solar plasma is partly ionized and the simple thermodynamical relations for an ideal gas do not apply. Owing to the corresponding changes in the thermodynamical properties of the matter up to 2/3 of the enthalpy flux is transported by latent heat and buoyancy driving of convective motions is strongly enhanced. Under the given conditions in the solar photosphere and the uppermost part of the convection zone it is sufficient to consider only the first ionization of the eleven most abundant elements in the Sun. The internal energy per mass unit  $\varepsilon_{\text{int}} = e_{\text{int}}/\varrho$  can be written as

$$\varepsilon_{\text{int}} = \frac{3}{2\varrho} (n_e + n_a) kT + \frac{1}{\varrho} \sum n_i^* \chi_i, \quad (10)$$

where the sum runs over the particle species,  $n_i^*$  is the number density of ionized particles of type  $i$ , and  $\chi_i$  is the corresponding ionization energy.  $n_a = \sum n_i$  is the number density of nuclei, and  $n_e$  the number density of electrons. Defining the ionization degree,  $x_i = n_i^*/n_i$ , and the relative abundance,  $\nu_i = n_i/n_a$ , (10) can be rewritten as

$$\varepsilon_{\text{int}} = \frac{3kT}{2\mu_a m_0} \left( 1 + \sum x_i \nu_i \right) + \frac{1}{\mu_a m_0} \sum x_i \nu_i \chi_i, \quad (11)$$

where  $\mu_a$  is the mean molecular weight of the neutral gas ( $\mu_a = 1.29$  for solar composition) and  $m_0$  is the atomic mass unit. The ionization degrees,  $x_i$ , are determined by the set of Saha equations

$$\frac{x_i}{1 - x_i} \sum x_i \nu_i = \frac{u_{i1}(T)}{u_{i0}(T)} \frac{\mu_a m_0}{\varrho} \frac{2(2\pi m_e kT)^{3/2}}{h^3} \exp(-\chi_i/kT). \quad (12)$$

The temperature dependence of the partition functions  $u_{i1}, u_{i0}$  can be obtained from the literature. For temperatures exceeding about 16,000 K, the

elements are almost fully ionized and the temperature dependence can be neglected. In order to obtain the temperature from  $\rho$  and  $e_{\text{int}}$ , the nonlinear system of equations (11) and (12) needs to be solved iteratively. Once the temperature is known, the gas pressure follows from the perfect gas equation:

$$p = (n_e + n_a) kT = \frac{\rho}{\mu_a m_0} \left( 1 + \sum x_i \nu_i \right) kT. \quad (13)$$

### 3 Numerical methods for radiative transfer

#### 3.1 The radiative source term

The photosphere is the region where most of the radiation leaves the Sun and where radiation takes over from convection as the dominant mechanism of energy transport. The energy exchange between gas and radiation determines the temperature structure of the photosphere and is responsible for the entropy drop which acts as the main driver of convection. Therefore any realistic simulation must include the radiative energy exchange rate,  $Q_{\text{rad}}$ , as a source term in the energy equation. Since the mean free path of photons increases strongly as the atmosphere becomes transparent in the photosphere, radiative transfer at this height becomes essentially non-local and a diffusion approximation of radiative energy transport as adequate for the solar interior cannot be applied.

The starting point for determining  $Q_{\text{rad}}$  is the (time- and frequency-dependent) radiative transfer equation (RTE hereafter),

$$\left( \frac{1}{c} \frac{\partial}{\partial t} + \mathbf{\Omega} \cdot \nabla \right) I_\nu = \kappa_\nu \rho (S_\nu - I_\nu) . \quad (14)$$

The specific intensity,  $I_\nu$ , is defined such that the amount of energy  $d\mathcal{E}_{\text{rad}}$  transported by radiation along direction  $\mathbf{\Omega}$  in the frequency interval  $(\nu, \nu + d\nu)$  across an area element  $dS$  into a solid angle  $d\omega$  in a time interval  $dt$  is

$$d\mathcal{E}_{\text{rad}} = I_\nu(\mathbf{x}, \mathbf{\Omega}, t) (\mathbf{\Omega} \cdot d\mathbf{S}) d\omega d\nu dt . \quad (15)$$

$S_\nu$  is the source function and  $\kappa_\nu$  is the frequency-dependent absorption coefficient of the material. Since the travel time of a photon through the photosphere is much shorter than any other relevant timescale, the radiation field can be assumed to adjust quasi-instantaneously to any change of the thermodynamical state of the gas, i.e. the time derivative in (14) can be neglected and we obtain:

$$\mathbf{\Omega} \cdot \nabla I_\nu = \kappa_\nu \rho (S_\nu - I_\nu) . \quad (16)$$

Defining the optical depth of a path element  $ds$  as  $d\tau_\nu = \kappa_\nu \rho ds$  the RTE for a given direction can be written in the form

$$\frac{dI_\nu(\boldsymbol{\Omega})}{d\tau_\nu} = S_\nu - I_\nu(\boldsymbol{\Omega}) , \quad (17)$$

which has the formal solution

$$I_\nu(\tau_\nu) = I_\nu(0) e^{-\tau_\nu} + \int_0^{\tau_\nu} S_\nu(t_\nu) e^{-(\tau_\nu - t_\nu)} dt_\nu . \quad (18)$$

In the case of local thermal equilibrium (LTE), the source function is given by the Planck function  $S_\nu = B_\nu$ . The essential premise of LTE is that elastic collisions between particles represent the dominant interaction on a microscopic level. Then the velocity distribution of particles is Maxwellian and the ionization states and population numbers of atomic, ionic, and molecular energy levels are determined by Saha-Boltzmann statistics corresponding to the local temperature. Significant departures from LTE must be expected in the upper photosphere, especially in strong spectral lines, for which scattering dominates over thermal emission and disturbs the detailed energy balance of LTE. This effect can be neglected as long as these lines do not contribute significantly to the total (frequency-integrated) energy exchange rate,  $Q_{rad}$ . Since in LTE the source function is independent of the radiation field, (18) can be integrated in a straightforward manner. The numerical treatment of radiative transfer is based on this formal solution. Once the radiation field is known, the radiative energy flux,

$$\mathbf{F}_\nu = \int I_\nu(\boldsymbol{\Omega}) \boldsymbol{\Omega} d\omega , \quad (19)$$

and the average intensity,

$$J_\nu = \frac{1}{4\pi} \int I_\nu(\boldsymbol{\Omega}) d\omega , \quad (20)$$

can be calculated. The radiative heating rate then follows either from

$$Q_{rad} = - \int_\nu (\nabla \cdot \mathbf{F}_\nu) d\nu \quad (21)$$

or from the equivalent expression

$$Q_{rad} = 4\pi\kappa_\rho \int_\nu \kappa_\nu (J_\nu - B_\nu) d\nu . \quad (22)$$

Consequently, for each cell in the computational grid, the numerical determination of the radiative heating rate,  $Q_{rad}$ , requires a sequence of integrations:

1. Spatial integration of the equation of radiative transfer (16) along a number of directions to determine the respective specific intensity  $I_\nu(\boldsymbol{\Omega})$ ,
2. angular integration of  $I_\nu(\boldsymbol{\Omega})$  to determine the radiative energy flux,  $\mathbf{F}_\nu$ , or the mean intensity  $J_\nu$ , and
3. frequency integration to determine the radiative heating rate from (21) or (22).

### 3.2 Radiative transfer on unstructured grids

In the course of our ANuME project in cooperation with the IAM of the University of Freiburg, we have carried out two studies on the spatial and angular integrations (steps 1 and 2 in the preceding section) in unstructured grids. The first study [1] concentrated on the modification of the short-characteristic formal solver [2] for the case of unstructured grids, while the second study [3] led to the development of a new class of adaptive solvers.

Ignoring the frequency dependence (to be discussed in Sec. 3.3) for the time being and thus dropping the index  $\nu$  in all frequency-dependent quantities, a short-characteristic solver starts from a discretized form of the formal solution (18) of the RTE. Consider the situation shown on the left panel of Fig. 2: given the incident intensity  $I_{i+1}$  at grid point  $i+1$ , characterized by optical depth  $\tau_{i+1}$  measured along the ray in the direction  $-\mathbf{\Omega}$  starting from  $\tau(s=\infty)=0$ , the intensity  $I_i$  is given by

$$I_i = I_{i+1} e^{-\Delta\tau_i} + \int_{\tau_i}^{\tau_{i+1}} S(\tau) e^{-(\tau-\tau_i)} d\tau, \quad (23)$$

where

$$\Delta\tau_i = \tau_{i+1} - \tau_i = \int_{s_{i+1}}^{s_i} \kappa(s)\rho(s) ds. \quad (24)$$

Accurate numerical evaluation of the integral in (23) would in general be cumbersome, but after approximating  $S(\tau)$  by a linear or quadratic function of  $\tau$ , it can be written analytically as

$$\Delta I = \int_{\tau_i}^{\tau_{i+1}} S(\tau) e^{-[\tau-\tau_i]} d\tau = \sum_{j=i-1}^{i+1} W_j S_j, \quad (25)$$

where the coefficients  $W_j$  depend only on the optical depth intervals,  $\Delta\tau_i$  and  $\Delta\tau_{i-1}$ . Approximating  $\kappa(s)$  by a linear or a quadratic function, (24) can also be replaced by a simple analytic expression in terms of the function values at the points  $i+1$ ,  $i$ , and  $i-1$ . Details of the method are described in [1].

The next step towards the determination of  $Q_{\mathbf{R}}$  is the integration of  $I(\mathbf{\Omega})$  over  $4\pi$  steradian of solid angle in order to obtain the mean intensity,  $J$ , or the radiative flux,  $\mathbf{F}$ . This integration is expressed as a quadrature sum over a discrete set of directions. The choice of the directions  $\mathbf{\Omega}_m$  and their weights  $w_m$  is subject to a few mandatory normalization criteria for the lowest moments of the intensity. In particular, the mean intensity  $J = \sum w_m I_m$  and the flux  $\mathbf{F} = 4\pi \sum w_m I_m \mathbf{\Omega}_m$  should obtain their correct values for an isotropic radiation field. A sensible criterion is the invariance under rotation around the  $z$ -axis over multiples of  $90^\circ$ . Another desirable criterion, although difficult to achieve, is that the directions should be distributed as evenly as possible over the entire sphere. An exact construction procedure of the angular quadrature has been given in [4]. It can be shown that, for a given quadrature,

the discretization errors in  $\mathbf{F}$  are markedly smaller than those in  $J$ . Errors are typically in the percent range for a quadrature with 3 directions per octant; significant improvements can only be achieved at a high computational cost.

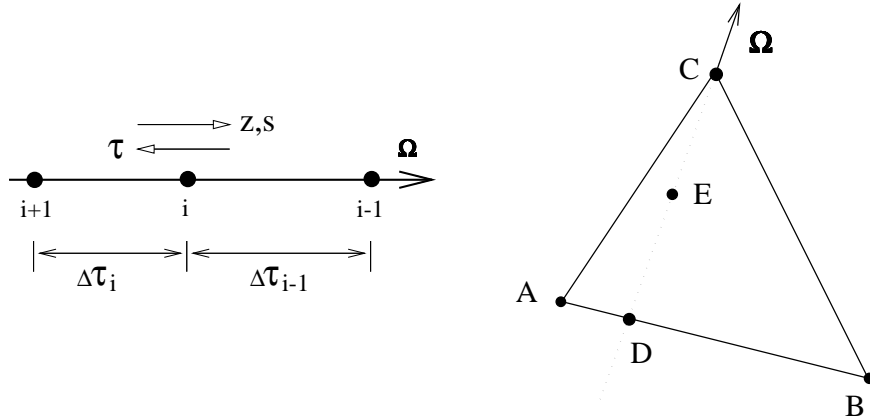


**Fig. 2.** *Left:* geometry for the short-characteristic solution of the radiative transfer equation in direction  $\Omega$ . *Right:* radiative transfer on a cell from a triangular grid. The specific intensity on corner C can be computed once the values on A and B are available for interpolation on point D (from [1]).

As an example for the adaptation of the short-characteristic method to a finite-volume scheme on an unstructured grid we consider the planar case with a triangular grid. The most obvious way to obtain  $Q_R$  would be through (20) by computing  $J$  directly for each cell center, but this straightforward approach requires excessive and poorly-defined interpolation. It is easier, more efficient, and more accurate to compute the intensities  $I$  at the vertices of the cells and afterwards use either  $J$  or  $\mathbf{F}$  to compute the cell-average of  $Q_R$  required by a finite-volume method.

First consider the radiative transfer problem within a single triangle (right panel of Fig. 2), where we want to compute  $I_C(\Omega)$ . The procedure is as follows: starting from C, tracing the ray in the upwind direction, locate point D where the ray enters the cell.  $I_C$  can be computed by means of a short-characteristic integration over the interval DC provided that the incident intensity  $I_D$  is known. In general, point D does not coincide with a vertex of the grid and  $I_D$  has to be interpolated from  $I_A$  and  $I_B$ , which must therefore be known beforehand: this requires that the intensities at the vertices are computed in the proper order. The incident intensities at the periodic side boundaries are obtained by iteration: from a suitable starting guess for the incident intensities at the vertices of the inflow boundary, compute the intensities at the corresponding vertices on the opposite boundary — which should be exactly

the same — and use those as update for the incident intensities. This process is repeated until the intensities have converged. Using iteration for the initialization, however, is tricky because the convergence rate of this iteration procedure can be slow in the optically thin part of the atmosphere. However, once the incident intensities have been initialized correctly, iteration can well be used to update the incident intensities after each time step; the outflow intensities at time  $t_n$  provide a good initial guess for the incident intensities at time  $t_{n+1}$ , so that few if any iterations are needed. The radiative transfer problem for the entire computational domain then simplifies to a sequence of radiative transfer problems on single triangles.

The simplest short-characteristic integration method uses  $\kappa_C$  and  $\kappa_D$  (the values of the opacity at point C and D, respectively) to define a linear relation  $\kappa(s)$  on the interval DC. Together with the relation for  $\rho(s)$  this yields an analytic expression for  $\Delta\tau_{DC}$ . That, in turn, is used together with  $S_C$  and  $S_D$  to define a linear relation  $S(\tau)$  to evaluate  $\Delta I$  from (23). This approach has limited applicability though: given the strongly non-linear dependence of  $\kappa$  on  $T$ , a small cell-to-cell variation of  $T$  already leads to significant non-linear variation of  $\kappa$ , so that the optical path length  $\Delta\tau_{DC}$  is misrepresented. Straight application of the short-characteristic method with quadratic  $S(\tau)$  is not possible, since it requires a point downwind from point C in order to define the necessary quadratic functions for  $\kappa(s)$  and  $S(\tau)$ . Such a point would be located outside of the triangle and violate the local character of the method. However, without significant adverse effects the method can be reformulated to use an auxiliary point E exactly halfway between D and C to define those quadratic functions. This quadratic approach significantly increases the maximum allowable cell-to-cell variation of  $T$  at a given accuracy level of  $I$ .

We have implemented radiative transfer routines to compute the radiative heating rate,  $Q_{\text{rad}}$  for various 2D model situations on a triangular grid [1].  $Q_{\text{rad}}$  can be computed from the mean intensity,  $J$ , or from the radiation flux,  $\mathbf{F}$ . We have studied the accuracy of the short-characteristic radiative solver on such a grid and the accuracy of the angular integration required to compute  $J$  and  $\mathbf{F}$ . It turned out that  $Q_{\text{R}}^J$  has severe accuracy problems in the optically thick regions while  $Q_{\text{R}}^F$  is stable and accurate there but may fail completely in optically thin layers. Therefore, the best solution is a combination of  $Q_{\text{R}}^J$  and  $Q_{\text{R}}^F$  with a selector based on the optical path lengths.

In a subsequent study in the course of the ANuME project, Dedner and Vollmöller [3] have compared a number of methods for the solution of the equation of radiative transfer on a triangular planar grid. These included the discontinuous-Galerkin finite element method [5], the long-characteristic method [6], and the short-characteristic method. All these methods can be generalized to the 3D case and to different grid geometries in a straightforward way. As a result of this study, a new class of methods was developed, the *extended-short-characteristic* (ESC) solvers, which combine the finite-element and short-characteristic approaches. In the case of triangles, the first-order version, ESC1, requires the determination of the intensity on the three node

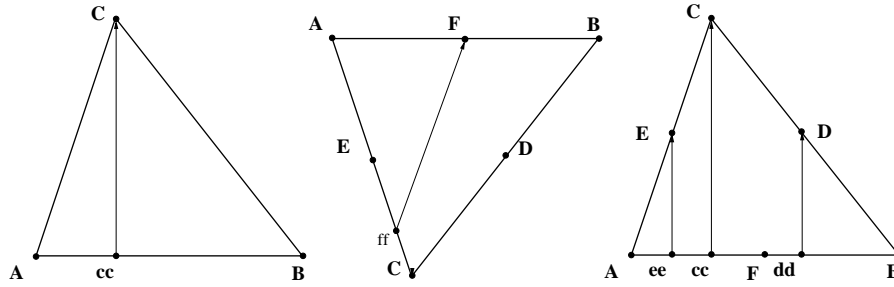


**Fig. 3.** To solve the RT equation on a single element using the extended-short-characteristic (ESC) method it is necessary to calculate the intensity for different points, depending on the desired order of the method (1 or 2) *Left:* in the ESC1 method the intensity at point C has to be computed on triangles with only one inflow edge along the characteristic starting at point cc. *Middle and right:* in the ESC2 method the intensities have to be computed at point F (two inflow edges) or E, C, D (one inflow edge) using the corresponding inflow intensities at point ff or at points ee, cc and dd respectively (from [3]).

points, while the second-order ESC2 method additionally includes the mid-points of the edges (see Fig. 3).

The ESC methods combine the idea of local ansatz functions for the solution from the finite element framework with the idea of solving local 1D initial value problems along characteristics. Variation of the ansatz functions allows to develop schemes of higher order. The method can be adapted to specific applications by using ODE solvers for RT equation which depend on the stiffness of the underlying ODE. Indeed it was found that Runge-Kutta solvers are superior to the classical formal solution approach with respect to the error-to-runtime ratio. To speed up the higher order ESC method, an adaptation strategy including the variation of the order from grid cell to grid cell is relatively simple to implement because the computation of the intensity coefficients is independent of the chosen ansatz function. In three space dimensions, the coefficients for the discrete solution are also given by the same ODE as in 2D, so that this part of the module can be used without modifications. Details about this study and the ESC methods can be found in [3].

### 3.3 Frequency-dependent radiative transfer

Since the total absorption coefficient (opacity) in the solar atmosphere comprises the effect of the order of  $10^6$  atomic and molecular spectral lines, a number of roughly  $10^6$ - $10^7$  frequency points is required to model the detailed frequency dependence. While this direct approach is feasible in calculating 1D static models, the computational cost is intolerable in time-dependent 2D or 3D simulations. The most radical simplification of the problem is achieved by

the grey approximation, replacing the frequency-dependent opacity by an averaged value, e.g. the Rosseland mean. The grey approach in combination with the diffusion approximation may be appropriate in the optically dense subphotospheric regions, where the radiation field is in local equilibrium with the gas, it is however unsatisfactory in the optically thinner regions where the radiation transfer becomes nonlocal. Here it is not only necessary to treat the full radiative transfer but also to incorporate line opacities, since line-blanketing effects have a considerable impact on both the photospheric dynamics and the emergent intensities. It is well known that the inclusion of line opacities in calculations of stellar model atmospheres strongly modifies the resulting temperature profiles, leading to considerably cooler outer layers, while the temperature is raised in deeper regions (the line cooling and backwarming effects). The effect of non-grey radiative transfer on the results of our MHD simulations has been studied in [7] and [8].

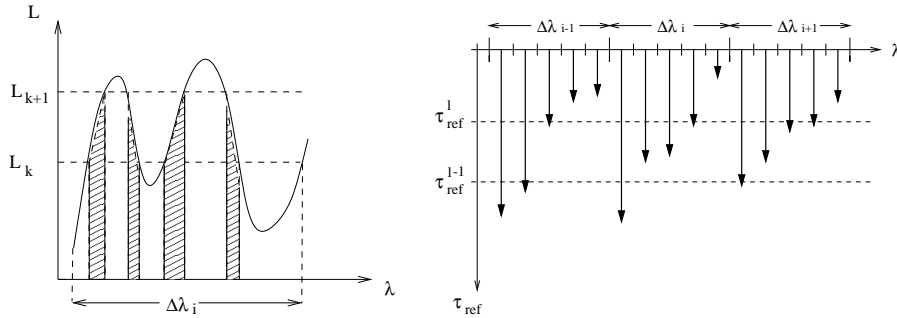


**Fig. 4.** *Left:* Sorting of wavelengths according to a discretization of opacity. The hatched areas mark those parts of the wavelength interval  $\Delta\lambda_i$  for which the opacity lies in the interval  $[L_k, L_{k+1}]$ . *Right:* Schematic illustration of the  $\tau$ -sorting procedure. The wavelength intervals  $\Delta\lambda_i$  are sorted to opacity bins according to the height where  $\tau = 1$  is reached for that wavelength interval, which is indicated by bold arrows (from [9]).

For reasons of computational feasibility in 2D/3D simulations, one has to resort to an appropriate statistical treatment of the line opacities that conserves the non-grey character of the radiation transport while drastically reducing the computational expense. In the context of time-dependent three-dimensional simulations, for which the radiative transfer must be solved for every timestep, the only feasible approach – given the computing resources of today – is the opacity binning approach, also called multi-bin or multi-group method [10, 11, 12]. The basic idea of this method is to sort frequencies into 4–6 (non-contiguous) groups according to the geometrical depth in a 1D reference atmosphere at which optical depth unity at that frequency is reached. For each of these frequency groups, a separate RT equation with group-integrated source function and opacity is solved and the respective intensities are then

added to obtain the total intensity. Under the assumption of local thermodynamic equilibrium (LTE), the (frequency-dependent) source function  $S_\nu$  is equal to the Planck function,  $B_\nu$ . The opacities can be then be obtained from pre-compiled tables without having to solve the system of rate equations for each gridpoint and timestep during a simulation run.

While the opacity binning approach has been tested in the case of 1D static model atmospheres [13], the application in the context of time-dependent 2D/3D simulations is accompanied by new sources of errors not encountered in the static 1D case like, for instance, strong lateral variations of the atmospheric properties and the occurrence of steep velocity gradients and shocks. In order to gain confidence in the applicability of this approach in simulations, we have performed in [9] a series of tests of the multigroup method for several 1D and 2D cases with the solution based on opacity distribution functions [14] serving as the reference solution.

In a plane-parallel atmosphere, a substantial improvement of the radiative heating rates in comparison to the grey case can be achieved with the multigroup method already with a moderate number of frequency groups. In order to test whether this result also holds for situations with substantial lateral variations, we have considered two cases: a magnetic flux sheet embedded in a non-magnetic atmosphere and a snapshot from a 2D simulation of solar surface convection.

### Magnetic flux sheet

We consider a simple model of a magnetic flux concentration, a 2D flux sheet. Using a 1D model atmosphere, the stratification in the interior of the sheet is shifted downwards by 200 km relative to the surrounding atmosphere, resulting in a strong lateral variation of the thermodynamic quantities. The width of the sheet as a function of height is determined by magnetic flux conservation together with the condition of total (magnetic plus gas) pressure equilibrium between the interior and the exterior of the sheet.

At the height  $z = 0$ , corresponding to the visible surface (continuum optical depth unity) in the exterior, the flux sheet has a width of 150 km. The sheet is fanning out with increasing height as the magnetic pressure necessary to balance the jump in gas pressure decreases. At the interfaces between the interior and the exterior of the sheet, the atmospheric parameters are smoothed horizontally over a distance of a few tens of kilometers by way of a Gaussian error function. Owing to the mirror symmetry of the sheet, the calculations can be restricted to one half of the flux sheet, with symmetrical boundary conditions imposed on the sheets symmetry axis (located at  $x = 0$ ). A Cartesian grid with  $201 \times 161$  grid points and horizontal and vertical resolutions of 2.5 km and 5 km, respectively, was used.

At equal geometrical height, density and temperature within the flux sheet are lower than the corresponding values in its surroundings. Consequently, the flux sheet is more transparent and thus subject to radiative heating from the

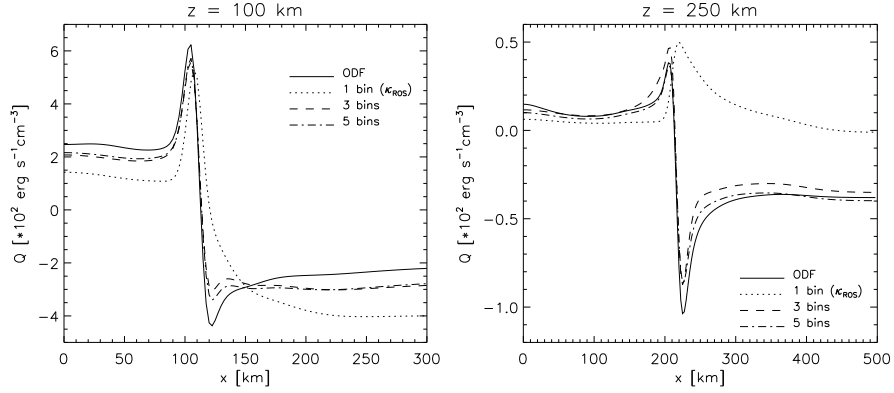


**Fig. 5.** Horizontal profiles of  $Q_{\text{rad}}$  at two different heights in a 2D atmosphere with an embedded flux sheet.  $x = 0$  corresponds to the symmetry axis of the sheet. The lines indicate the reference solution (obtained using opacity distribution functions, the grey solution (1 bin, Rosseland opacity) and the solutions for opacity binning with 3 and 5 bins, respectively (from [9]).

hot ‘walls’ of surrounding plasma. This can be seen in Fig. 5, which shows the radiative heating rate,  $Q_{\text{rad}}$ , as a function of the horizontal coordinate for two geometrical heights. The grey (Rosseland opacity) and multi-group results are compared with the reference solution based upon an opacity distribution function (ODF) description of the spectrum with effectively nearly 4000 frequency points. Corresponding to the horizontal temperature gradient, a heating peak inside the sheet and a stronger cooling region outside form near the sheet boundary. Below  $z \simeq -150$  km, the outside atmosphere and most of the boundary region are optically thick and the radiative transfer is essentially grey, so that  $Q_{\text{rad}}$  is well represented even without a detailed treatment of the frequency dependence. The maximum relative errors near the heating and cooling peaks range between 5 and 10 percent.

At  $z = 100$  km (left panel of Fig. 5), both multi-group solutions qualitatively reproduce the ODF case while the grey case is much less accurate. The heating peak at the boundary is shifted outwards by approximately 10 km, the peak value being reduced by 15 percent with respect to the ODF case, while the small cooling dip outside is not captured at all. At a still greater height of 250 km (right panel of Fig. 5), both the 3- and 5-bin approximations yield acceptable results, though neither captures the full extent of the cooling peak outside the sheet boundary. The grey solution, on the other hand, does not even approximately reproduce the reference solution. The heating peak *inside* the sheet has vanished; instead, heating takes place immediately *outside* the sheet, where the reference solution shows considerable cooling. This behavior can be explained by the fact that, on the basis of the Rosseland mean, the interior of the sheet is transparent at a height of 250 km; accordingly, the

interaction between gas and radiation is very weak within the sheet, resulting in small values of  $Q_{\text{rad}}$ . In the optically thicker regions immediately outside the sheet, radiation originating from deeper, hotter regions at the *opposite* sheet boundary and crossing the sheet almost unattenuated, leads to a net heating effect. This example clearly demonstrates how important a nongrey approach to radiative transfer can be in optically thin regions in order to obtain accurate values of  $Q_{\text{rad}}$ . It also shows that the multi-group approach leads to a reasonably adequate description of the non-grey effects.

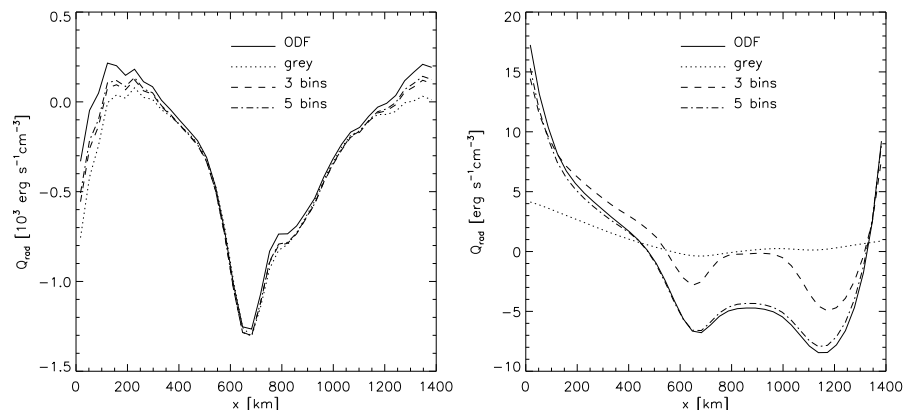


**Fig. 6.** Horizontal profiles of  $Q_{\text{rad}}$  for a snapshot from a 2D simulation of solar convection at heights of 100 km (left panel) and 500 km (right panel) above the visible solar surface (from [9]).

### Convection simulation

As a further step towards more realistic situations we tested the opacity binning models with a snapshot from a 2D simulation of solar surface convection [15], which has no relation to the one-dimensional reference atmosphere used for sorting the frequencies into groups. The vertical and horizontal extent of the computational domain is  $1400 \times 1400 \text{ km}^2$  with a grid resolution of 35 km. Fig. 6 shows  $Q_{\text{rad}}$  in horizontal cuts at heights of approximately 100 and 500 km above the visible solar surface, respectively. Similar to results for the flux sheet, all solutions (including the grey case) agree reasonably well with each other in the deeper layers, although the errors of the grey case become more pronounced towards the horizontal boundaries of the domain. The differences between the 3- and 5- bin solutions are only marginal. At 500 km height, the grey solution completely fails to reproduce the reference solution while the 5-bin solution excellently matches the reference curve.

In summary we can conclude that our test calculations have shown that the multi-group approach yields a good approximation to the frequency-integrated

radiative heating rate at moderate computational cost, which makes it the method of choice in multidimensional time-dependent MHD simulations. The advantage over the grey approximation is particularly pronounced in situations which deviate strongly from the one-dimensional plane-parallel case. In these cases the radiative transfer is complicated by lateral heating and cooling effects. Grey radiative transfer often fails to capture these effects, which leads to qualitatively wrong heating rates in the upper photosphere. This is particularly relevant if magnetic field concentrations are included, since the partial evacuation of these structures leads precisely to the kind of lateral inhomogeneities which are not well modeled by the grey approach. The test calculations with snapshots from numerical simulations have shown that the good performance of the multi-group method does not strongly depend on the choice of the reference atmosphere, which underlines the applicability of this method in realistic multi-dimensional simulations.

## 4 Simulations results for solar magneto-convection

In the course of the ANumE project, we have developed two codes for the simulation of radiative MHD. The MHD part of the first code (called IAM-MPAe code in what follows) is due to our partners at the IAM (University of Freiburg) and incorporates Riemann solvers for real gases and unstructured grids. We have implemented the ESC solvers for radiative transfer in the 2D version of this code, calculated the tables of the (non-ideal) equation of state, and introduced a realistic open boundary condition at the bottom of the computational box. This code has then be used to follow the formation of magnetic flux concentrations in the solar atmosphere and to analyze their oscillation properties [16]. Some of these results are summarized in Sec. 4.1.

The MHD part of the second code has been jointly developed with colleagues from the University of Chicago. We have introduced a short-characteristic radiative transfer solver including a non-grey treatment based upon the multi-group method [7], partial ionization, and an open lower boundary. Results from simulations runs with this code (the MURAM<sup>1</sup> code) are given in Sec. 4.2.

### 4.1 Convective intensification of magnetic flux

Observations show that the majority of the magnetic flux through the solar atmosphere is assembled in magnetic field concentrations with a field strength of 1500 G and above [17]. Such field strengths exceed the value  $B_{\text{eq}}$  corresponding to equipartition between magnetic energy density and kinetic energy density of the convective flows by at least a factor of three. Consequently, the concentration of the magnetic flux cannot be solely due to the passive advection of

---

<sup>1</sup>MPAe and University of Chicago **RA**diation **M**HD code

magnetic field lines by converging convective motions until the Lorentz force impedes further transport.

It has been suggested that thermodynamic effects play an important role for the intensification of the magnetic field beyond the equipartition limit,  $B_{\text{eq}}$ . The suppression of the horizontal convective motion once the field strength approaches  $B_{\text{eq}}$  throttles the energy supply to the magnetic regions. Since at the solar surface the radiative energy loss into free space continues, this leads to a substantial cooling of the gas. Under the influence of gravity and pressure forces, the cool and dense gas sinks down. The downflow is further accelerated by the convectively unstable (strongly superadiabatic) stratification below the solar surface. This leads to a partial evacuation of the upper part of the forming flux concentration, which becomes laterally compressed by the external pressure until the field has grown strong enough to reestablish lateral pressure equilibrium. The combination of processes of flux advection by horizontal flow, suppression of convection, radiative cooling, downflow and compression is called *convective collapse* or *convective intensification* [18, 19, 20, 21].

We have used the 2D version of the adaptive IAM-MPAe code to study the convective intensification of magnetic flux in a region of 12,000 km horizontal size extending in the vertical direction between 300 km above and 900 km below the visible solar surface. The computational setup is to start with a slightly perturbed plane-parallel convectively unstable stratification and let non-magnetic convection develop until a statistically stationary situation is reached. Then a homogeneous vertical magnetic field of 100 Gauss is introduced and its development followed in the course time.

Fig. 7 (to be found in the section with color pages at the end of this volume) shows a sequence of snapshots of the magnetic field (field lines) and the temperature field (color coding), which clearly demonstrates the concentration of the magnetic field into a few intense flux sheets of kilogauss field strength located in convective downflow regions. The simulations nicely confirm the theoretical concepts of flux expulsion and convective collapse. Within a few minutes, most of the magnetic flux is transported by the converging horizontal flows to the cool downflow region (flux expulsion). Suppression of the convective energy transport and ongoing radiative cooling leads to downflow of the gas in the flux concentrations. The reduced internal pressure leads to lateral compression by the external gas pressure, resulting in a strong intensification of the field strength to kilogauss values. About 20 minutes after the introduction of the magnetic field, the flux concentrations have merged into three large flux sheets, which govern the surrounding flow pattern with strong downflows surrounding the flux sheets. After about 30 minutes this quasi-stationary situation has fully developed.

Figure 8 shows the temporal evolution of the average field strength in magnetic flux sheet I in Fig. 7 near the visible solar surface. Two stages of field amplification can be seen: first, a rapid concentration of the field to about 1 kG by flux expulsion and radiative cooling within the first 3-4 minutes after the introduction of the magnetic field, which is followed by a second, slower

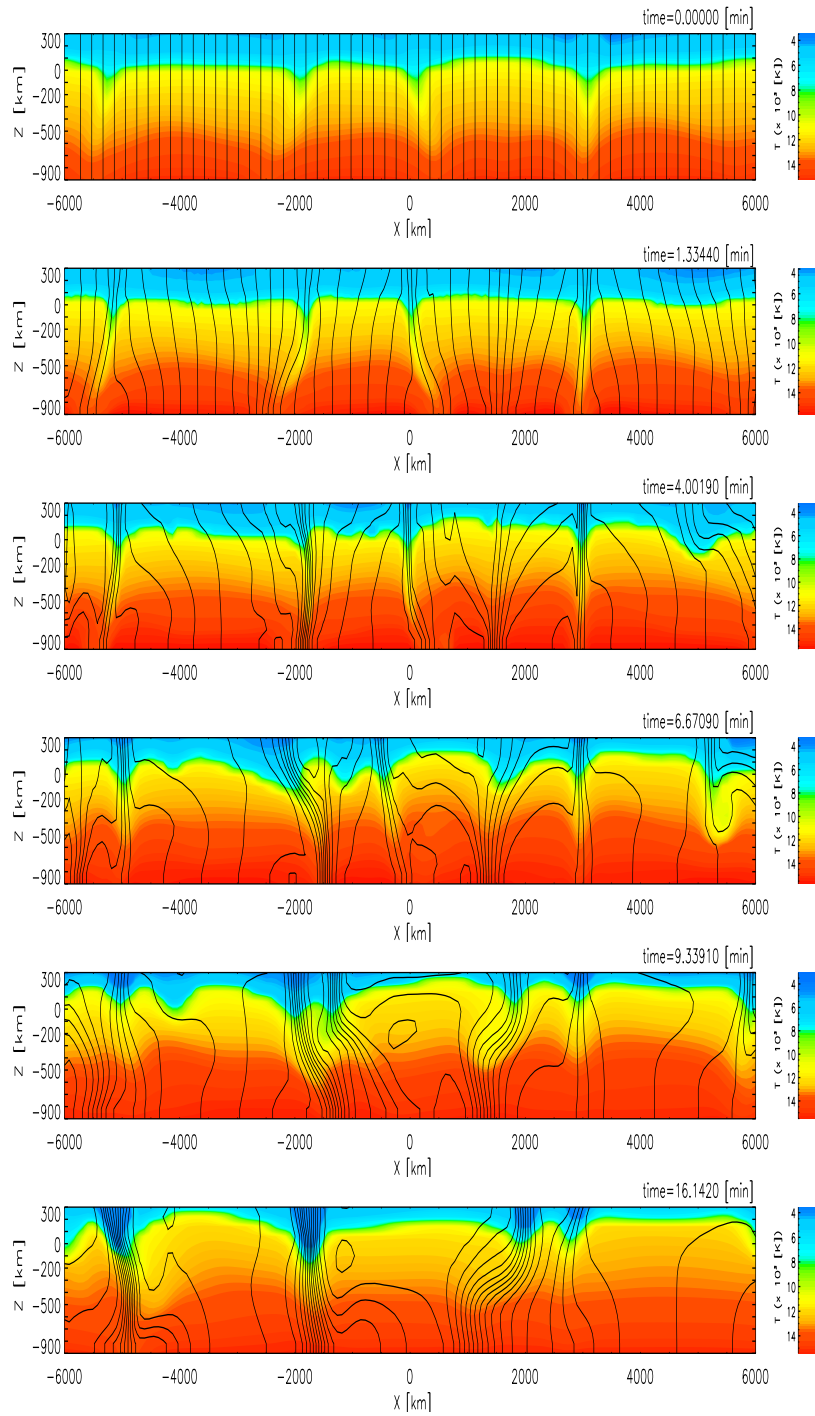
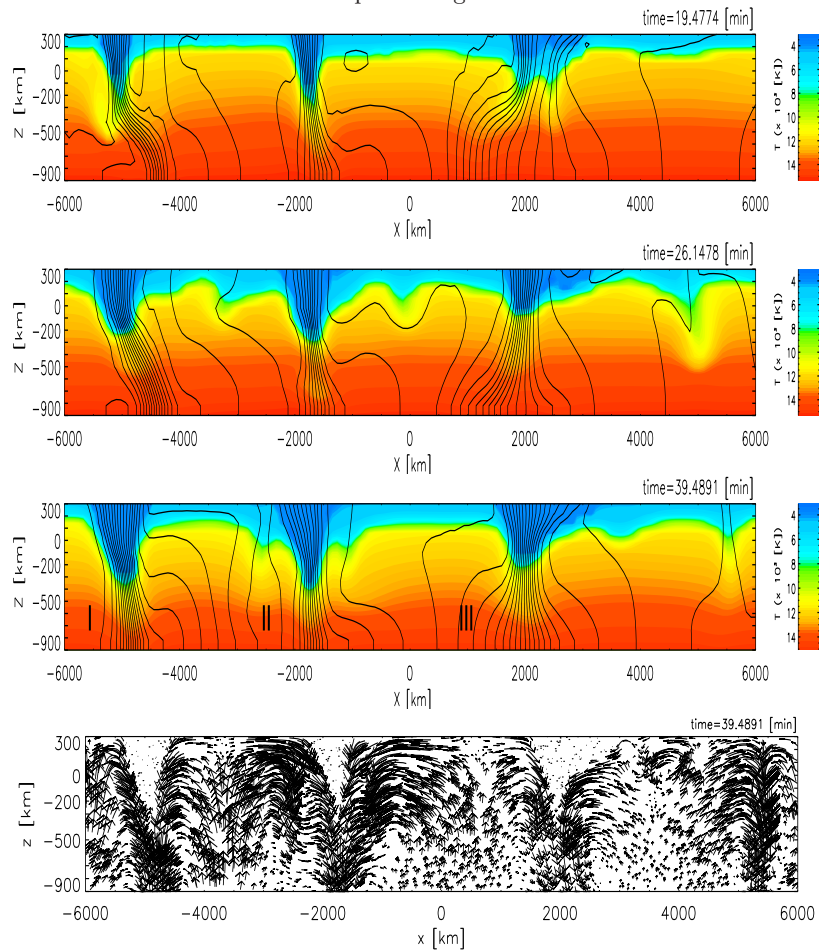
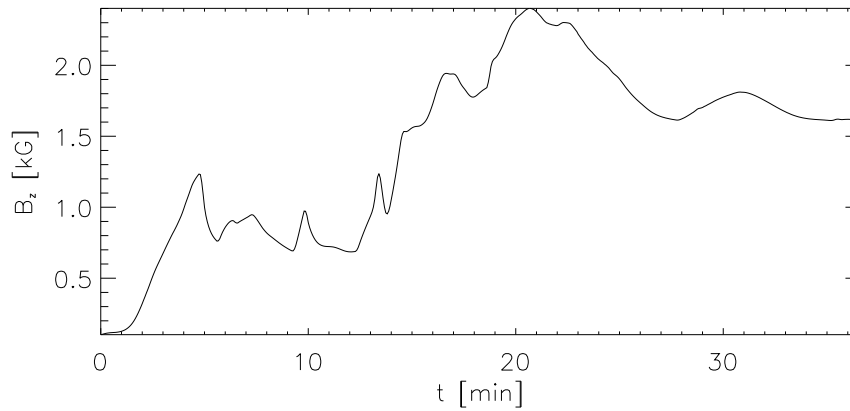


Fig. 7. to be continued

sequel to Fig. 7.



**Fig. 7.** Time evolution of magnetic field (field lines are shown in black) and temperature (color coded) from a 2D simulation run of solar magneto-convection near the visible solar surface (located at  $z \simeq 100$  km height). A homogeneous vertical field of 100 Gauss has been introduced at  $t = 0$  after a statistically stationary convection pattern has evolved. Within a few minutes, most of the magnetic flux is transported by the converging horizontal flows to the cool downflow region (flux expulsion). Owing to the suppression of the convective energy transport, the gas in the flux concentrations cools and sinks; lateral compression by the external gas pressure then leads to a strong intensification of the field strength, which reaches kilogauss values. About 20 minutes after the introduction of the magnetic field, the flux concentrations have merged into three large flux sheets (labeled **I,II,III**), which start to determine the surrounding flow pattern with strong downflows surrounding the flux sheets. After about 30 minutes a quasi-stationary situation has developed. The velocity field in this state is shown in the form of velocity vectors in the last panel (from [16]). (See also color figure, Plate 11.)



**Fig. 8.** Temporal evolution of the magnetic field strength for the magnetic flux sheet **I** in Fig. 7 at a geometrical height roughly corresponding to the visible solar surface. The field is intensified to about 1 kilogauss within a few minutes by the combined action of flux expulsion by the convective flow and radiative cooling. The continuing downflow within the magnetic flux concentration leads to further evacuation and amplification of the field to values around 2 kilogauss.

increase of the field due to a persistent downflow and evacuation of the upper layers of the flux sheet. The second process leads to field strengths around 2 kG.

## 4.2 Formation of dynamic magnetic structure

### The MURAM code

The study of the full dynamics of the solar magnetic structure requires realistic simulations in three dimensions. As an intermediate step before the full completion of the 3D version of the IAM-MPAe code by implementation of a non-grey radiative transfer module (ongoing work, to be finished in 2004), we have developed the MURAM code. This code allowed us to carry out simulation runs with a full non-grey radiative transfer module in 3D. The MURAM code solves the MHD and RT equations on a three-dimensional regular Cartesian grid with constant grid spacing. The spatial derivatives are discretized with 4th-order centered differences on a  $5^3$  point stencil. Time stepping is explicit with a 4th-order Runge-Kutta solver. The scheme is stabilized by the application of shock-resolving diffusion and hyperdiffusivity [22], which prevent the build-up of energy at scales comparable to the size of the grid cells. These artificial diffusivities assume significant values only near discontinuities and in regions of unresolved waves while those regions which are well resolved remain largely unaffected by diffusion. For the equation of state the instantaneous ionization equilibrium for the first ionization of the 11 most abundant

elements is considered. The relevant thermodynamic quantities are stored in tables from which the required values are interpolated during a simulation run.

The bottom boundary conditions implemented in the MURAM code permit free in- and outflow of matter and maintain a constant mass in the box as well as a fixed energy flux through the system. In the present version of the code, the top of the domain is closed with stress-free boundary conditions for the horizontal velocity components; the implementation of a more realistic transmitting upper boundary is under development. The magnetic field is assumed to be vertical at the top and bottom boundaries, the footpoints of fieldlines are allowed to move freely. The horizontal directions are taken to be periodic in all variables.

The code is parallelized by means of domain decomposition. The computational domain is divided into a three-dimensional array of subdomains, each of which is endowed with two layers of ghost cells at its boundaries as required by the 4th-order spatial discretization scheme. We use message passing (MPI) for parallel computers with distributed memory.

The radiative transfer equation is solved for each frequency set determined by opacity binning and for each direction using the short characteristic scheme with linear or parabolic interpolation of opacity and source function as well as linear interpolation of density. In the context of the domain decomposition used for parallelization, the short characteristic scheme requires an iteration for each ray direction and each frequency set. For a given ray direction the scheme starts in each subdomain at those boundaries through which the radiation enters (the ‘upwind’ boundaries). The intensity values at these boundaries are assumed to be known. Then the traversal of the subdomain proceeds in the downwind direction, systematically moving away from the upwind boundaries, thus making sure that the upwind intensities required for the interpolation are always known. However, on those upwind boundaries of a subdomain which do not coincide with the top or bottom boundary of the computational box, the intensities are a priori unknown. Therefore, the scheme is iterated until convergence at the boundaries is obtained. After each iteration the intensities at a given upwind boundary are updated with the new values provided by the neighboring subdomain. We found that 2 to 3 iteration steps per frequency set and direction are usually sufficient, if one chooses as initial guess for the intensities on the upwind boundaries a linear extrapolation of the values of the previous two time steps.

More details about and further results obtained with the MURAM code can be found in [7, 23, 24, 25].

### **Simulation of a solar plage region**

A plage region (cf. Fig. 1) is a strongly magnetized part of the solar atmosphere outside sunspots (but often in their vicinity) with a horizontally averaged field strength of about 200 G. We have carried out a simulation run in a

computational box corresponding to a height of 1400 km and  $6000 \times 6000 \text{ km}^2$  width on the Sun, discretized with a spatial grid of  $100 \times 288 \times 288$  points.

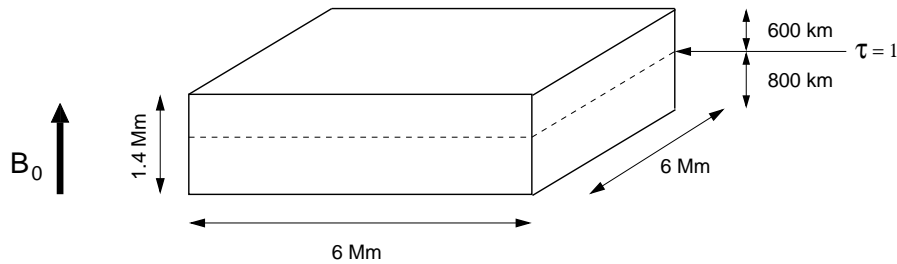


**Fig. 9.** Geometrical setup of the simulation runs with the MURAM code. The vector  $\mathbf{B}_0$  indicates the vertical homogeneous magnetic field introduced into the hydrodynamic convection at the beginning of the magnetic phase.

Similarly to the 2D runs described in the previous section, the simulations with the MURAM code were started as non-magnetic convection. After the convection had fully developed and reached a statistically stationary state (about one hour solar time after the start of the simulation), a homogeneous vertical initial magnetic field of field strength  $B_0$  was introduced. Here we show results from a run with  $B_0 = 200 \text{ G}$ , corresponding to a solar plage region.

Within a few minutes of simulated time (approximately one turnover time of the convection) most of the magnetic flux has been transported to the downflow lanes of the convective granulation pattern and intensified to kilogauss field strength. For a snapshot taken about 2 hours solar time after the start of the magnetic phase, Fig. 10 shows the vertical magnetic field, vertical velocity, and temperature distributions on a horizontal plane corresponding roughly to the visible solar surface. In addition, the frequency-integrated intensity (brightness) is shown on the lower right panel. The magnetic map shows sheet-like magnetic structures extending along convective downflow lanes, while larger structures with diameters of up to 1000 km appear at the vertices where several downflow lanes merge. Typical field strengths in these field concentrations are between 1500 and 2000 G.

The network of magnetic structures is organized on a ‘mesoscale’ which typically comprises 4–6 convective upflow regions (granules). While this magnetic pattern is rather stable (it evolves on a time scale of hours), the small-scale pattern of the field concentrations is highly time-dependent, with magnetic flux being constantly redistributed within the magnetic network. In the intensity map shown in Fig. 10, the larger flux concentrations appear dark owing to the reduced efficiency of convective energy transport. There is a considerable small-scale variation of the intensity within the pore-like flux concentrations, which is related to localized hot upflows in regions of reduced

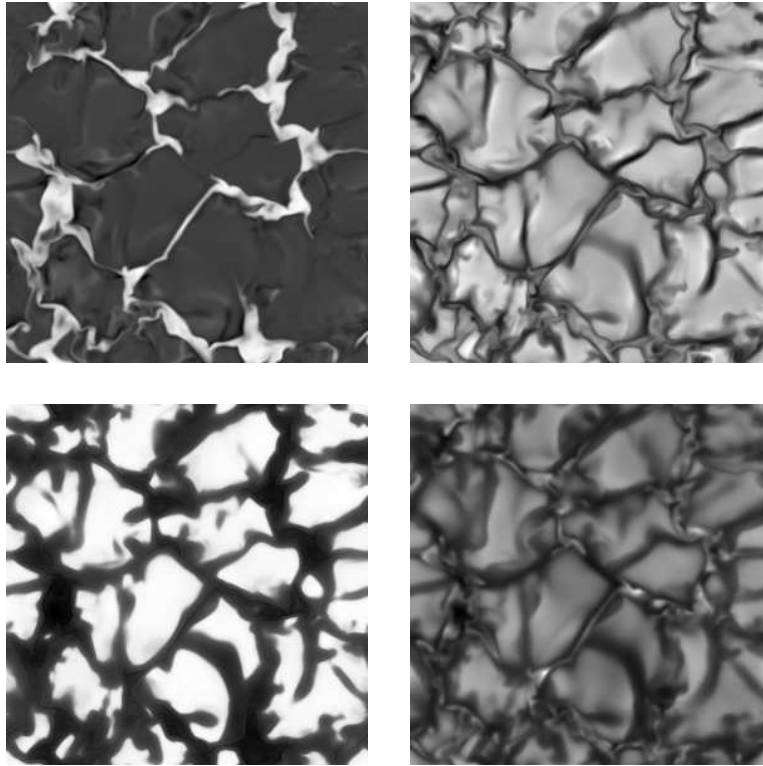


**Fig. 10.** Snapshot from the simulation of a solar plage region ( $B_0 = 200$  G) with the MURAM code. Brightness map (lower right) and horizontal cuts near the visible solar surface of vertical magnetic field component (upper left), vertical velocity component (upper right) and temperature (lower left). Light and dark shades indicate higher and lower values, respectively. The velocity plot shows convective upflows shaded in light grey separated by intergranular downflow lanes. In the magnetic-field plot, the strong sheet- and pore-like magnetic field concentrations appear in white.

field strength. In the thin sheets, lateral heating effects in combination with the depression of the level of optical depth unity lead to a brightening with respect to the surrounding downflow regions (see Fig. 11).

Fig. 12 shows some statistical properties of the simulation run from a series of statistically independent snapshots (i.e., with a temporal cadence exceeding the granule lifetime). A horizontal slice consisting of 8 grid layers (corresponding to a thickness of 112 km), which include the visible solar surface, served as the basis for the analysis.

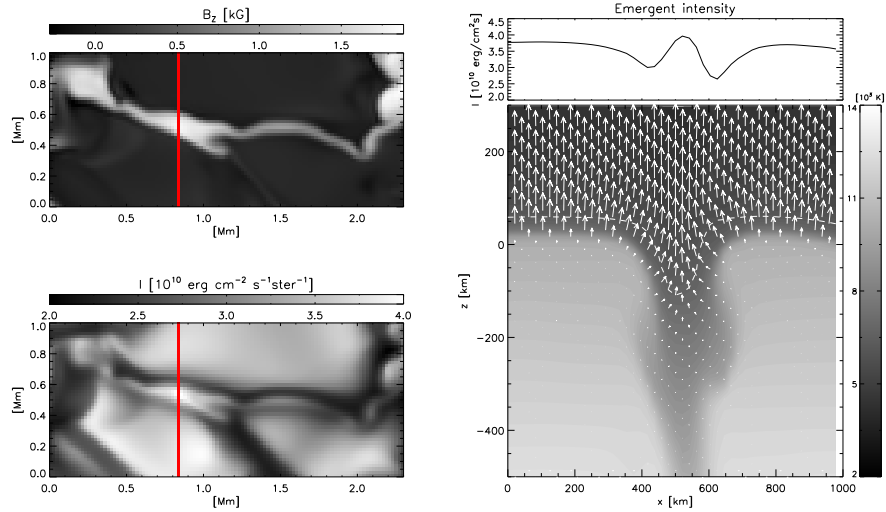


**Fig. 11.** Radiative properties of a sheet-like magnetic structure in a convective downflow lane. *Left:* vertical field strength (top) and brightness (bottom). The vertical line indicates the position of the cut shown on the right panel. *Right:* grey-shading of the the temperature distribution in a vertical cut, together with the radiative flux vectors. There is an influx of radiation from the hot walls of the flux sheet into its partially evacuated cooler interior. The radiative heating leads to enhanced brightness (shown at the top), so that the flux sheet appears as a bright structure within the darker downflow lane.

The probability distribution function (PDF) for the magnetic field, signed with the orientation of its vertical component is shown in the upper left panel of Fig. 12. It shows a superposition of two components. Most of the volume considered is occupied by weak field, the probability density dropping off approximately exponentially with increasing field strength. The distribution reveals a pronounced local minimum at  $B = 0$ , indicating that the magnetic field, albeit being mostly weak, permeates the whole volume and field-free regions are largely avoided. Superimposed on this exponential distribution is a Gaussian “bulge” (the high field strength wing showing the characteristic parabolic shape on a logarithmic scale) with a maximum around 1500 G, which reflects the sheet- and pore-like structures in the network of concentrated magnetic field.

The correlation diagram (joint PDF) of magnetic field strength and inclination angle of the field vector with respect to the horizontal plane given in the upper right panel of Fig. 12 shows that most of the strong field above the kilogauss level is vertical and upward directed (which is the orientation of the homogeneous initial field), presumably as the result of buoyancy forces acting on the partially evacuated magnetic structures. The inclination angle of weak

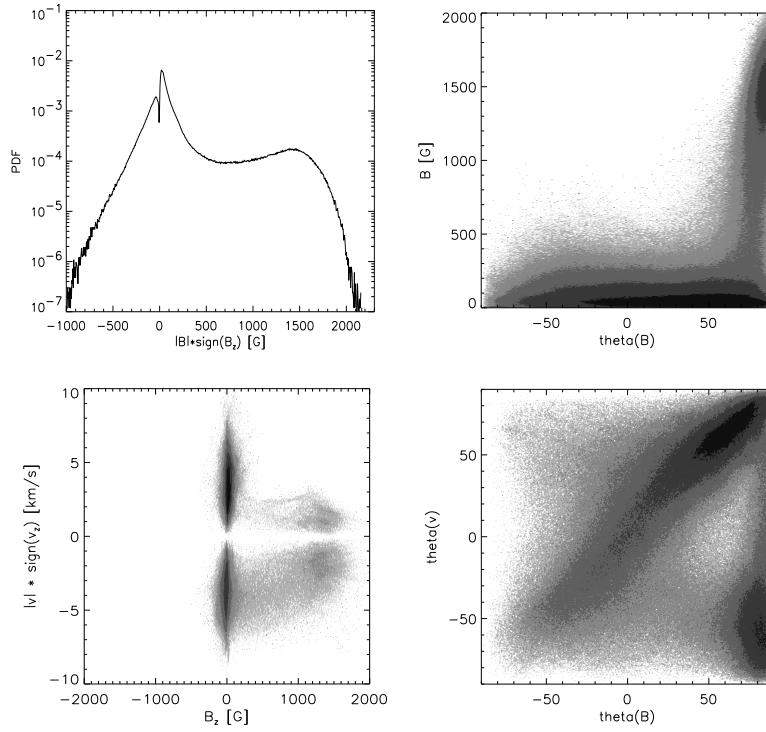


**Fig. 12.** Statistical properties of a layer of about 110 km thickness around the visible solar surface. *Upper left:* probability distribution (PDF) of the field strength, signed with the vertical orientation of the field vector. *Upper right:* joint PDF of field strength and the inclination angle of  $\mathbf{B}$  with respect to the horizontal,  $\text{theta}(\mathbf{B})$ . *Lower left:* joint PDF of flow velocity, signed with its vertical orientation, and field strength. *Lower right:* joint PDF of the inclination angles of the flow,  $\text{theta}(\mathbf{v})$ , and of the magnetic field,  $\text{theta}(\mathbf{B})$ . The grey-scaling indicates the probability density on a logarithmic scale.

fields is much more evenly distributed. With decreasing field strength a slight preference for upward directed fields is observed.

The joint PDF of the vertical magnetic field and the flow velocity signed with the vertical orientation of the flow in the lower left panel of Fig. 12 (positive velocities correspond to upflows) shows the effect of strong fields on the fluid motions: while flow velocities up to  $8 \text{ km s}^{-1}$  can be found in weak field regions, the amplitudes of fluid motions are reduced in magnetic structures with field strengths above 1000 G. Fluid motions are not completely suppressed, however, since the predominantly vertical fields leave vertical fluid motions largely unaffected. Downflows are preferred inside strong field features.

The lower right panel of Fig. 12 shows the joint PDF of the inclination angles of magnetic field vector and flow vector with respect to the horizontal plane. The pronounced diagonal lobe indicates that in most of the volume considered flow field and magnetic field are more or less aligned. In addition to this component, one observes a strong correlation of (strong) vertical magnetic field with downflows.

### Further simulations and studies

We have already carried out a number of further simulations with the MURAM code and used the results to study various physical processes on the Sun. Among these investigations are:

1. A study of the quantitative effects of the frequency-dependent radiative transport on the simulation results. It turns out that the non-grey treatment leads to significantly smaller temperature fluctuations, particularly in the upper photosphere. This leads to brightness contrasts in agreement with observational values [8].
2. A parameter study of magneto-convection with different amount of vertical magnetic flux in the box ranging from  $B_0 = 10$  G ('quiet' Sun),  $B_0 = 50$  G,  $B_0 = 200$  G (the plage region described in the foregoing section), to  $B_0 = 800$  G. As the average field strength increases, the magnetic flux concentrations become larger and the field increasingly affects and eventually dominates the convective motions (Vögler et al., publication in preparation)
3. Simulations of larger magnetic structures in the solar photosphere. Such darkish 'pores' with diameters of a few Mm represent the transition from small, bright flux concentrations to dark sunspots. The questions investigated are: how is a pore held together, how is it affected by energy transport along the field, how does it interact with the surrounding convection? Further studies concern the atmospheric structure (temperature, pressure) within a pore and its observational signatures (Cameron et al., publication in preparation).
4. A comparison of the fractal dimension of the magnetic field pattern in the simulations with observations of the magnetic structure in the solar photosphere. There is a remarkable agreement between simulation and observation, increasing the confidence in the 'realism' of the simulations [26].
5. A study of the brightness of magnetic flux concentrations when observed in spectral bands dominated by molecular lines, particularly in Fraunhofer's 'G band' with many spectral lines from the CH molecule. Through the comparison of synthetic images from simulation results with actual observations, the physical mechanism leading to the brightness contrast of magnetic structures could be unveiled. The evacuated and heated magnetic flux concentrations show lower abundances of CH, leading to less

absorption in spectral lines and thus larger brightness. These results put the indirect approach of studying of the magnetic field dynamics in the solar atmosphere by observing bright features in the G band on a firm physical basis [27].

6. An investigation of the evolution of an initial field with mixed polarity, i.e., half of the initial magnetic field pointing upward and the other half downward. This permits the temporal decay of unsigned magnetic flux by reconnection of field lines and cancellation of opposite polarity flux. By running simulations with various horizontal distributions of the initially vertical field (half-by-half, two-by-two,...) and determining the decay rate, it is possible to determine values of the ‘turbulent’ magnetic diffusivity, which is a very important quantity for studies of the long-term evolution of the magnetic flux at the solar surface. Furthermore, the results of such simulation runs are compared with observations of the magnetic field dynamics in regions of mixed polarity on the Sun (Keller et al., publication in preparation).
7. The various tools developed for spectroscopic and polarimetric analysis to compare the simulation results with actual solar measurements have been applied to various magneto-convection simulations. The analysis of these results and the comparison with observations reveals rich diagnostic information in good agreement with measurements, which is used to identify the physical processes behind the observational phenomena (Shelyag et al., publications in preparation).

## 5 Summary & Outlook

Our work on the ANumE project(s) has proven to be very fruitful. We have developed and tested methods to incorporate radiative transfer into MHD simulations and to take account of the frequency dependence of radiation in a stellar atmosphere. State-of-the-art codes have been developed and successfully applied to simulate magneto-convection in the solar atmosphere. With the MURAM code we have a fully working 3D code for realistic simulations, which has already produced a wealth of useful results. This code is our present ‘workhorse’ and several ongoing projects exploit its rich possibilities and analyze data produced by this code, often in direct comparison with observational results.

Further development of the MURAM code will include introducing a transmitting boundary condition at the top and using a non-uniform grid in the vertical direction with a grid spacing proportional to the average pressure. This will allow us to extend the computational box in the vertical direction.

Work on the 3D version of the IAM-MPAe code still continues and we expect to have a complete version with radiative transfer in mid 2004. Comparison runs with the MURAM code will allow us to optimize the grid refinement strategy and will also provide a mutual test of both codes. The

IAM-MPAe code will then be used to attack the challenging physical questions of the higher solar atmosphere, in particular the chromosphere, which is dominated by interacting MHD shock waves. The IAM-MPAe code with its Riemann solvers and adaptive mesh refinement is perfectly suited for such kind of environment.

*Acknowledgement.* We would like to thank Andreas Dedner, Dietmar Kröner, Christian Rohde, and Matthias Wesenberg, our partners from the Institute of Applied Mathematics (IAM), University of Freiburg, for a fruitful cooperation during the ANumE programme. We are grateful to Fausto Cattaneo, Thierry Emonet, and Timur Linde from the University of Chicago for their contributions to the development of the MURAM code. We thank the coordinator of ANumE, Prof. G. Warnecke and his staff for much support and for the management of the programme. Last, but not least, we thank the Deutsche Forschungsgemeinschaft (DFG) for generous support of our project Schu 500/7 and all the DFG staff involved with ANumE and with our project in particular for their efficient, friendly, and non-bureaucratic dealing with our sometimes non-standard requests.

## References

1. Bruls, J. H. M. J., Vollmöller, P., Schüssler, M.: Computing radiative heating on unstructured spatial grids. *Astron. Astrophys.*, **348**, 233–248 (1999)
2. Kunasz, P. B., Auer, L.: Short characteristic integration of radiative transfer problems: formal solution in two-dimensional slabs. *J. Quant. Spectrosc. Radiat. Transfer*, **39**, 67–79 (1988)
3. Dedner, A., Vollmöller, P.: An Adaptive Higher Order Method for Solving the Radiation Transport Equation on Unstructured Grids. *Journal of Computational Physics*, **178**, 263–289 (2002)
4. Carlson, B. G.: The numerical theory of neutron transport. In B. Alder and S. Fernbach (eds) *Methods in Computational Physics* **1** (1963)
5. Lesaint, P., Raviart, P. A.: On a finite element method for solving the neutron transport equation. In: C. de Boor (ed) *Mathematical Aspects of Finite Elements in Partial Differential Equations*, Academic Press, New York, pp. 89–123 (1974)
6. Mihalas, D., Auer, L. H., Mihalas, B. R.: Two-dimensional radiative transfer. I - Planar geometry. *Astrophys. J.*, **220**, 1001–1023 (1978)
7. Vögler, A.: Three-dimensional simulations of magneto-convection in the solar photosphere. PhD thesis, University of Göttingen (2003)
8. Vögler, A.: Effects of non-grey radiative transfer on 3D simulations of solar magneto-convection. *Astron. Astrophys.*, **421**, 755–762 (2004)
9. Vögler, A., Bruls, J. H. M. J., Schüssler, M.: Approximations for non-grey radiative transfer in numerical simulations of the solar photosphere. *Astron. Astrophys.*, **421**, 741–754 (2004)
10. Nordlund, A.: Numerical simulations of the solar granulation. I - Basic equations and methods. *Astron. Astrophys.*, **107**, 1–10 (1982)
11. Ludwig, H.-G., Jordan, S., Steffen, M.: Numerical simulations of convection at the surface of a ZZ Ceti white dwarf. *Astron. Astrophys.*, **284**, 105–117 (1994)

12. Skartlien, R.: A Multigroup Method for Radiation with Scattering in Three-Dimensional Hydrodynamic Simulations. *Astrophys. J.*, **536**, 465–480 (2000)
13. Ludwig, H.-G.: Nichtgrauer Strahlungstransport in numerischen Simulationen stellarer Konvektion. PhD thesis, University of Kiel, Germany (1992)
14. Kurucz, R. L.: Model atmospheres for G, F, A, B, and O stars. *Astrophys. J. Suppl. Ser.*, **40**, 1–340 (1979)
15. Ploner, S. R. O., Solanki, S. K., Gadun, A. S.: The evolution of solar granules deduced from 2-D simulations. *Astron. Astrophys.*, **352**, 679–696 (1999)
16. Vollmöller, P.: Untersuchung der Wechselwirkung von Magnetfeldkonzentrationen und konvektiven Strömungen mit dem Strahlungsfeld in der Photosphäre der Sonne. PhD thesis, University of Göttingen (2001)
17. Solanki, S. K.: Small scale solar magnetic fields - an overview. *Space Sci. Rev.*, **63**, 1–188 (1993)
18. Spruit, H. C., Zweibel, E. G.: Convective instability of thin flux tubes. *Sol. Phys.*, **62**, 15–22 (1979)
19. Parker, E. N.: Hydraulic concentration of magnetic fields in the solar photosphere. VI - Adiabatic cooling and concentration in downdrafts. *Astrophys. J.*, **221**, 368–377 (1978)
20. Roberts, B., Webb, A. R.: Vertical motions in an intense magnetic flux tube. *Sol. Phys.*, **56**, 5–35 (1978)
21. Schüssler, M.: Theoretical Aspects of Small-Scale Photospheric Magnetic Fields. In J. O. Stenflo (ed) *Solar Photosphere: Structure, Convection and Magnetic Fields*, IAU Symposium 138, Kluwer, Dordrecht, pp. 161–179 (1990)
22. Caunt, S. E., Korpi, M. J.: A 3D MHD model of astrophysical flows: Algorithms, tests and parallelisation. *Astron. Astrophys.*, **369**, 706–728 (2001)
23. Vögler, A., Shelyag, S., Schüssler, M., Cattaneo, F., Emonet, Th., Linde, T.: Simulation of solar magneto-convection. In: N. E. Piskunov, W. W. Weiss, and D. F. Gray (eds) *Modelling of Stellar Atmospheres*, ASP Conf. Series, Astronomical Society of the Pacific, San Francisco, pp. 157–168 (2003)
24. Vögler, A., Schüssler, M.: Studying magneto-convection by numerical simulation. *Astron. Nachr./AN*, **324**, 399–404 (2003)
25. Schüssler, M.: MHD simulations: what's next? In: J. Trujillo Bueno and J. & Sánchez Almeida (eds) *Third International Workshop on Solar Polarization*, ASP Conf. Ser., Astronomical Society of the Pacific, San Francisco, pp. 601–613 (2003)
26. Janßen, K., Vögler, A., Kneer, F.: On the fractal dimension of small-scale magnetic structures in the Sun. *Astron. Astrophys.*, **409**, 1127–1134 (2003)
27. Schüssler, M., Shelyag, S., Berdyugina, S., Vögler, A., Solanki, S. K.: Why Solar Magnetic Flux Concentrations Are Bright in Molecular Bands. *Astrophys. J.*, **597**, L173–L176 (2003)